Progress in Nuclear Energy 122 (2020) 103262

Contents lists available at ScienceDirect

Progress in Nuclear Energy

journal homepage: http://www.elsevier.com/locate/pnucene

A processing method of generating $S(\alpha, \beta, T)$ tables considering resonance elastic scattering kernel for the Monte Carlo codes

Tiejun Zu *, Jialong Xu, Liangzhi Cao

School of Nuclear Science and Technology, Xi'an Jiaotong University, Xi'an, Shaanxi, 710049, China

ARTICLE INFO

Keywords:
Resonance elastic scattering kernel
Nuclear data processing
$S(\alpha$
β
$T)$
NECP-Atlas

ABSTRACT

It has been proved that resonance elastic scattering kernel (RESK) has significant impact on the energy and angle distributions of the secondary neutrons, and consequently affects the eigenvalues and fuel temperature coefficients. Therefore, it is necessary for the nuclear data processing codes to generate the accurate data considering RESK for the neutronics analysis. In this paper, a processing method is proposed to generate the $S(\alpha, \beta, T)$ tables efficiently for Monte Carlo codes to account for the RESK. A multi-point linearization method is developed to generate the incident energy grids of $S(\alpha, \beta, T)$ tables, which can minimize the data size of $S(\alpha, \beta, T)$ tables without losing accuracy. The equally probable cosines in $S(\alpha, \beta, T)$ tables are obtained by solving the sets of nonlinear equations which are established by Legendre polynomials and the differential moments of RESK. The generation procedure of the $S(\alpha, \beta, T)$ tables is more practical by using the proposed calculation method of equally probable cosines. Based on the proposed processing method, a new module is developed in the nuclear data processing code called NECP-Atlas. The ACE-format libraries with the $S(\alpha, \beta, T)$ tables are generated by NECP-Atlas and supplied to the OpenMC code to perform the verifications. The numerical results show that the impact on eigenvalues caused by the RESK can be reflected correctly by the Monte Carlo calculations using the $S(\alpha, \beta, T)$ tables. Meanwhile, the results based on the $S(\alpha, \beta, T)$ tables match well with those based on the Doppler broadening rejection correction approach.

1. Introduction

In the epi-thermal energy range, the thermal agitation of target nuclei will cause up-scattering of the secondary neutrons, in other words, it has important impact on the energy and angle distributions of secondary neutrons, i.e. the scattering kernels. Especially, for the heavy nuclides with strong resonance elastic scattering within the epi-thermal energy range, the scattering kernels are deeply dependent on the resonance structures. The scattering kernel affected by the resonance elastic scattering is known as the resonance elastic scattering kernel (RESK) (Ouisloumen and Sanchez, 1991). RESK has a great impact on the neutronics simulations, which leads the eigenvalues, fuel temperature coefficients and other neutronics parameters quite different from those based on the conventional asymptotic scattering kernel (Dagan, 2005; Becker et al., 2009; Mori and Nagaya, 2009; Zoia et al., 2013). Therefore, the nuclear data processing codes, which are used to generate cross section libraries for the neutronics simulation codes, should provide accurate RESK data.

For the deterministic based neutron analysis, the multi-group cross sections and scattering matrices are required in the neutron transport calculations. Besides the scattering matrices which are affected by RESK, the multi-group cross sections can also be affected, since the neutron energy spectra used as the weighting functions to evaluate the cross sections are changed when RESK is considered. Some researchers have proposed several methods to account for RESK in the calculation of the multi-group data including cross sections and scattering matrices. In the works (Lee et al., 2008; He et al., 2016), the correction factor method is applied to correct the multi-group data, where the correction factors are generated by the Monte Carlo codes which can accurately treat RESK. In the works (Ghrayeb et al., 2014; Ouisloumen et al., 2015), the accurate scattering matrices are provided by directly integrating the formulae of RESK (Ouisloumen and Sanchez, 1991) with the numerical methods, and the ultra-fine group structure (more than 6000 groups) is used to reduce the effect of RESK on weighting functions. Besides, a method has been developed by the authors of the present paper (Xu et al., 2019), which can calculate the scattering matrices based on the two-dimensional interpolation tables of RESK, and the multi-group cross sections using the neutron energy spectra considering up-scattering

* Corresponding author.
E-mail addresses: tiejun@xjtu.edu.cn (T. Zu), sd3296708@126.com (J. Xu), caolz@mail.xjtu.edu.cn (L. Cao).

https://doi.org/10.1016/j.pnucene.2020.103262
Received 9 January 2019; Received in revised form 16 October 2019; Accepted 19 January 2020
Available online 7 February 2020

effect. In this method, a relatively coarse multi-group structure such as EPRI-CPM-69 group structure can be used to generate multi-group data with high accuracy.

For Monte Carlo codes, there are two methods having been used to account for RESK in the neutron transport simulation. One is using the Doppler broadening rejection correction (DBRC) approach and the other is using the $S(\alpha, \beta, T)$ tables. The DBRC approach is a sampling method used for exactly simulating the elastic collision between neutrons and target nuclei (Becker et al., 2009; Becker, 2010; Dagan et al., 2011; Walsh et al., 2014). The DBRC approach needs to be implemented into the Monte Carlo codes so that the correct energy and angle distributions of secondary neutrons can be simulated in the Monte Carlo calculations.

For the Monte Carlo (MC) codes with the DBRC approach unavailable, the $S(\alpha, \beta, T)$ tables is an alternative method to consider RESK. The initial purpose of using the $S(\alpha, \beta, T)$ tables in the MC calculations is to capture the scattering kinematics of neutrons scattered from the bound molecules such as the hydrogen in water. The $S(\alpha, \beta, T)$ tables given in ACE library includes three key points, i.e. the incident energy grids, the scattering kernels of 0^{th} Legendre order for each incident energy and the equally probable cosines at each secondary energy. Theoretically, the $S(\alpha, \beta, T)$ tables can also be used to capture the scattering kinematics of neutrons in the epi-thermal energy range where RESK is dominant. The $S(\alpha, \beta, T)$ tables were generated initially based on the double differential cross sections whose derivation is given by the researchers (Rothenstein, 2004; Dagan, 2005). Although the methods of generating the $S(\alpha, \beta, T)$ tables (Rothenstein, 2004; Dagan, 2005) have theoretical feasibility, there are some limitations when the methods are applied to nuclear data processing codes. In the work (Rothenstein, 2004), it is pointed out that tremendous piecewise functions must be numerically integrated if the converged double differential cross sections are desired. Meanwhile, the $S(\alpha, \beta, T)$ tables are dependent on the temperatures, so it is very time-consuming to generate the tables. Besides, the research (Becker, 2010) has illustrated that the incident energy grid in the $S(\alpha, \beta, T)$ tables should capture the resonance structure of individual nuclide, so that the incident energy grid should be carefully set, considering both the efficiency and accuracy. While in the work (Dagan, 2005), the generation of $S(\alpha, \beta, T)$ tables was performed on a fixed fine incident energy grid depended on the resonance structure of ^{238}U. If the $S(\alpha, \beta, T)$ tables of other heavy nuclides are generated based on the fixed fine incident energy grid based on ^{238}U, the accuracy of the $S(\alpha, \beta, T)$ tables cannot be guaranteed.

In the present work, a processing method is proposed to generate the $S(\alpha, \beta, T)$ tables, which can avoid the limitations mentioned above. Firstly, a linearization method called multi-point linearization method is proposed to generate incident energy grids of $S(\alpha, \beta, T)$ tables adaptively according to the resonance structures of the target nuclides. The data size of $S(\alpha, \beta, T)$ tables is minimized and the accuracy of $S(\alpha, \beta, T)$ table for any nuclide can be guaranteed. Secondly, a calculation method is proposed to calculate the equally probable cosines without utilizing the double differential cross sections. The equally probable cosines are obtained by solving the sets of equations which are established by the Legendre polynomials and the differential moments. The calculation of differential moments is based on the analytical and semi-analytical integration methods adopted in the previous work (Xu et al., 2019). The computational cost of differential moments is much lower than that of double differential cross sections based on piecewise integration, which can greatly accelerate the generation of $S(\alpha, \beta, T)$ tables.

This paper is organized as follows. In Section 2, the processing methods are described. In Section 3, the numerical results are demonstrated. The conclusions are given in the last section.

2. Methodologies

In this section, the new processing methods for generating the $S(\alpha, \beta, T)$ tables will be introduced. According to the descriptions in the previous section, there are three key points to produce the $S(\alpha, \beta, T)$ tables, i.e. the incident energy grids, the scattering kernels of 0^{th} Legendre order at each incident energy and the equally probable cosines at each secondary energy. In the present work, the methods for generating the incident energy grids and calculating the equally probable cosines will be described, while the calculation method of the scattering kernels of 0^{th} Legendre order is identical as the previous work (Xu et al., 2019), so it will be demonstrated briefly.

2.1. Brief introduction for the calculation method of the RESK

The formula of the RESK(Ouisloumen and Sanchez, 1991) is given by

$$\sigma_{sn}^{T}(E \to E') = \frac{\beta^{5/2}}{4E}\exp(E/kT)\int_0^{\infty} t\sigma_{s,0}\left(\beta\frac{kT}{A}t^2\right)\exp\left(-t^2/A\right)\psi_n(t)dt, \quad (1)$$

with

$$\beta = (A+1)/A, \quad (2)$$

where t is a variable proportional to the neutron speed; $\sigma_{s,0}$ is the tabulated 0 K cross section; k is Boltzmann's constant; T is the temperature of the material; A is the ratio of the nucleus mass to the mass of the neutron.

2.2. Then, the $\psi_n(t)$ is represented as

$$\begin{aligned}\psi_n(t) = {} & H(t_+ - t)H(t - t_-), \\ & \times \int_{\varepsilon_{\max}-t}^{t+\varepsilon_{\min}} \exp\left(-x^2\right)Q_n(x,t)dx + H(t - t_+) \\ & \times \int_{t-\varepsilon_{\min}}^{t+\varepsilon_{\min}} \exp\left(-x^2\right)Q_n(x,t)dx\end{aligned} \quad (3)$$

with

$$t_{\pm} = \frac{\varepsilon_{\max} \pm \varepsilon_{\min}}{2}, \quad (4)$$

and

$$\varepsilon_{\max} = \sqrt{(A+1)\max(E,E')/kT}, \quad (5)$$

$$\varepsilon_{\min} = \sqrt{(A+1)\min(E,E')/kT}. \quad (6)$$

where H is the Heaviside step function.

2.3. Finally, $Q_n(x,t)$ is given by

$$Q_n(x,t) = \frac{4}{\sqrt{\pi}}\int_0^{2\pi} P_n(\mu_{lab})P(\mu_{CM})d\varphi, \quad (7)$$

where

$$\mu_{CM} = \frac{1}{4x^2t^2}(A + B\cos\varphi), \quad (8)$$

and

$$\mu_{lab} = \frac{1}{4x^2\varepsilon_{\max}\varepsilon_{\min}}(C + B\cos\varphi), \quad (9)$$

with

$$A = \left(\varepsilon_{\max}^2 - x^2 - t^2\right)\left(\varepsilon_{\min}^2 - x^2 - t^2\right), \quad (10)$$

$$C = \left(\varepsilon_{\max}^2 + x^2 - t^2\right)\left(\varepsilon_{\min}^2 + x^2 - t^2\right), \quad (11)$$

and

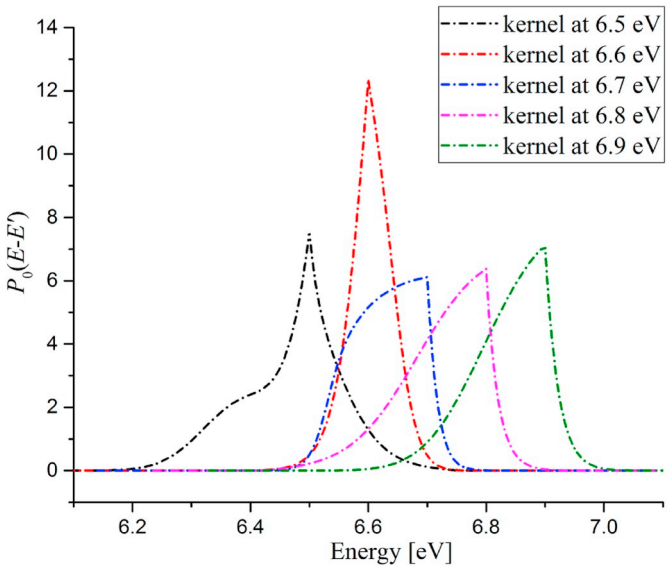

Fig. 1. The scattering kernels of 0th Legendre order of ^{238}U for the incident energy from 6.50 eV to 6.90 eV.

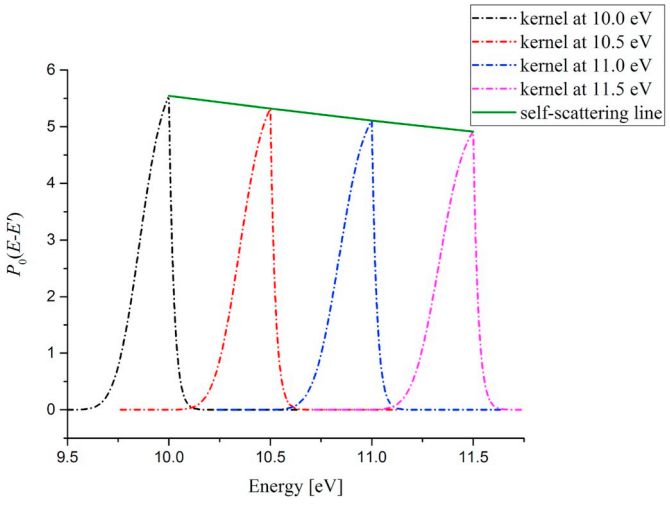

Fig. 2. The scattering kernels of 0th Legendre order of ^{238}U for the incident energy from 10.00 eV to 11.50 eV.

$$B = \left[(t+x)^2 - \varepsilon_{\max}^2\right]\left[(t+x)^2 - \varepsilon_{\min}^2\right]\cdot \times\left[\varepsilon_{\max}^2 - (t-x)^2\right]\left[\varepsilon_{\min}^2 - (t-x)^2\right] \quad (12)$$

From the above formulae, it can be observed that Eq. (1) is a triple integral. For the third fold of the integral (i.e. Eq. (7)), it is evaluated analytically. For the second fold of the integral (i.e.Eq. (3)), it is evaluated based on different Legendre orders. For the first two orders, the second fold of integral can be represented as a relatively simple analytical expression. For the higher orders, the analytical expression is quite complicated, so the integral is evaluated numerically. As for the first fold of the integral, the integral is calculated by using piece-wise numerical integration.

2.4. Generation method of the incident energy grid

In the previous section, it is demonstrated that the $S(\alpha, \beta, T)$ tables should be generated on particular incident energy grids in order to capture the resonance structure of individual nuclide. Based on the numerical analysis, it is observed that the shapes of scattering kernels

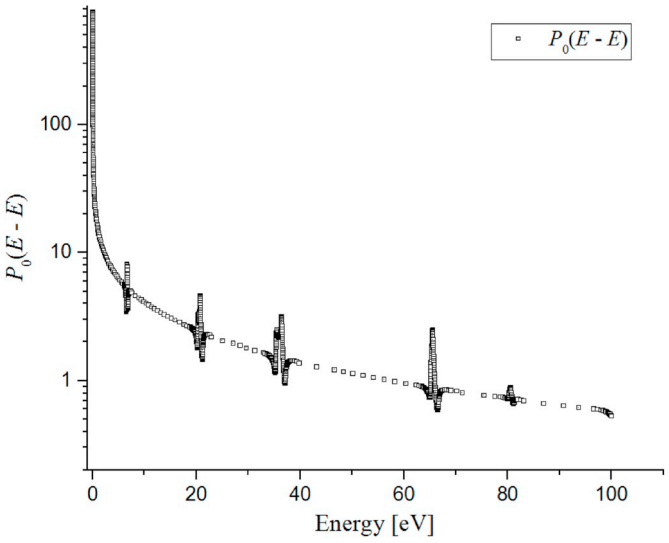

Fig. 3. The self-scattering probabilities of 0th Legendre order of ^{238}U at 900 K for the incident energy from 1E-5 eV–100 eV.

vary drastically when the incident energies are close to the resonance peaks, and vary smoothly when the incident energies are away from the resonance peaks. Fig. 1 shows 5 scattering kernels of 0th Legendre order of ^{238}U at 293.6 K for the incident energies of 6.50 eV, 6.60 eV, 6.70 eV, 6.80 eV and 6.90 eV. Each dashed line represents an individual scattering kernel and the points constructing the lines are the scattering probabilities. These 5 incident energy points are close to 6.67 eV where the first s-wave resonance peak of ^{238}U is located. It can be observed that the shapes of the scattering kernels at different incident energies change drastically. Fig. 2 shows 4 scattering kernels of 0th Legendre order of ^{238}U at 293.6 K for the incident energies of 10.00 eV, 10.50 eV, 11.00 eV and 11.50 eV, and these 4 incident energy points are away from the first (6.67 eV) and second (20.87 eV) s-wave resonance peaks. It can be noticed that the shapes of the scattering kernels change smoothly, and the values of self-scattering probabilities (the highest point on each dashed line in Fig. 2) show linear relationship with incident energies (the green solid line in Fig. 2). It means that it is unnecessary to use too much incident energy points in the region where no resonance peaks are located, and several scattering kernels can represent their variation trend. Based on this point, a linearization method was proposed in the previous work (Xu et al., 2019), where the incident energy grid is obtained by linearizing the values of self-scattering probability with a given tolerance. Fig. 3 shows the self-scattering probabilities of 0th Legendre order of ^{238}U at 900 K for the incident energy from 1E-5 eV–100 eV. And the incident energy points corresponding to the self-scattering probabilities construct the incident energy grid. The positions where the curve changes drastically are energy points where the first five s-wave resonance peaks are located. At the positions around the resonance peaks, the incident energy points are relatively fine due to the fast change of the scattering kernels as mentioned above. Away from the resonance peaks, the incident energy points are relatively sparse.

The above linearization method can guarantee the precision of interpolated scattering probabilities near the incident energy. During our farther research, a phenomenon is found that the precision of scattering probabilities obtained by interpolation may decrease when the secondary energies are away from the incident energy. And this phenomenon only happens when the incident energy is relatively low. Fig. 4 and Fig. 5 show the comparisons of the scattering probabilities of ^{238}U at 900 K for the incident energy of 2E-5 eV and 4E-5 eV, respectively. It can be seen that the values of interpolated scattering probabilities cannot match with those obtained by theoretic calculation. The numerical results shows that the eigenvalues and temperature coefficients are hardly

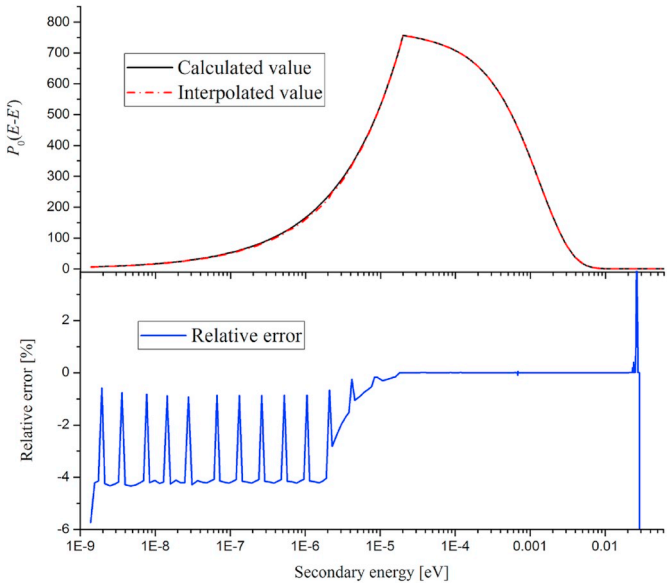

Fig. 4. The comparison of the scattering probabilities of ^{238}U for the incident energy of 2E-5 eV.

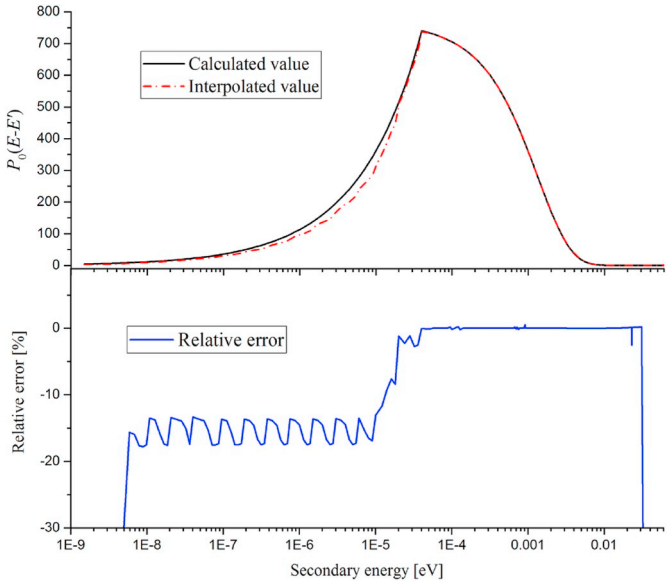

Fig. 5. The comparison of the scattering probabilities of ^{238}U for the incident energy of 4E-5 eV.

affected despite of the large interpolation error shown in Figs. 4 and 5. But for the nuclear data processing, this kind of phenomenon indicates that the robustness of the above linearization method is not strong. Therefore, to enhance the robustness of the above linearization method and avoid the potential error, we propose a new linearization method.

The new linearization method is called multi-point linearization method and it not only makes the self-scattering probability can be linearly interpolated with a given tolerance, but also the scattering probabilities at other secondary energy points. In the multi-point linearization method, more secondary energy points are set to judge whether the interpolated values of scattering probabilities match with the theoretic calculation results under the given tolerance. In order to define the energy points used for judgement, the area of the secondary energy is divided into two parts: the down-scattering part and up-scattering part. Several energy points are set in each parts, and the numbers of the secondary energy points located in both parts are the same. Besides, the incident energy point is also used to judge the convergence. In the down-scattering part, the logarithmic energy decrement Δu_{down} from incident energy E to the minimum secondary energy $E'_{\min}$ is defined as

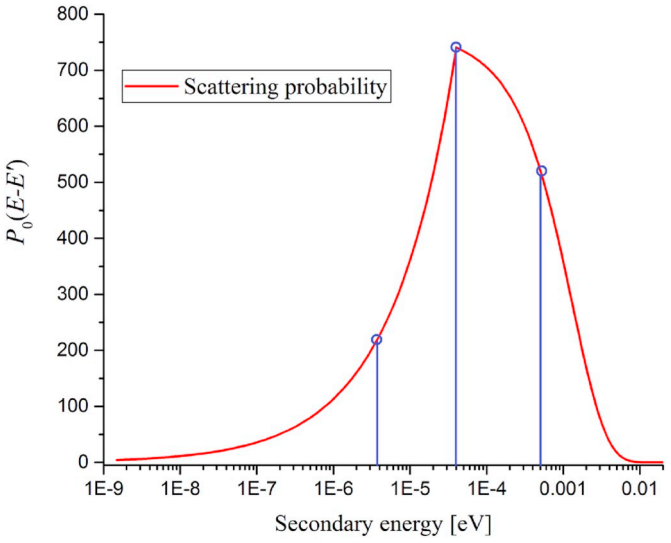

Fig. 6. The definition of the secondary energies for multi-point linearization.

$$\Delta u_{down} = \ln\left(\frac{E}{E'_{\min}}\right), \tag{13}$$

where $E'_{\min}$ is derived based on the two-body kinematics assuming the target velocity follows Maxwellian distribution. Then, Δu_{down} is divided into N equal widths and there are N-1 points of division defined as the secondary energy points in the down-scattering part. The secondary energy points in the down-scattering part are represented as

$$E'_{down,L} = \frac{E}{\exp\left(\frac{\Delta u_{down}}{N}\right)\cdot L}, \qquad L = 1, 2, \ldots, N-1, \tag{14}$$

where $E'_{down,L}$ is the L^{th} secondary energy point in the down-scattering part.

Similarly, in the up-scattering part, the logarithmic energy decrement Δu_{up} from the maximum secondary energy $E'_{\max}$ to the incident energy E is defined as

$$\Delta u_{up} = \ln\left(\frac{E'_{\max}}{E}\right), \tag{15}$$

where $E'_{\max}$ is derived based on the two-body kinematics assuming the target velocity follows Maxwellian distribution. Then, Δu_{up} is divided into N equal widths and there are N-1 points of division defined as the secondary energy points in the up-scattering part. The secondary energy points in the up-scattering part are represented as

$$E'_{\text{up},L} = E \cdot \exp\left(\frac{\Delta u_{up}}{N}\right)\cdot L, \qquad L = 1, 2, \ldots, N-1, \tag{16}$$

where $E'_{up,L}$ is the L^{th} secondary energy point in the up-scattering part.

Take Fig. 6 as example, there are one secondary energy point defined in the down-scattering part and up-scattering part, respectively. There are three secondary points in all used for linearization judgement (i.e. the points where the blue lines cut the abscissa). The blue circles represent the scattering probabilities corresponding to the secondary energies.

After describing the method for setting secondary energy points to check the interpolation error, the linearization process is performed, as

the following steps.

1) Set an initial incident energy grids to divide the whole incident energy range into a series of intervals. In general, it is obtained from the energy grids of the tabular cross sections at 0 K.
2) Check whether the linearization tolerance is satisfied for the energy intervals one by one from low energy to high energy. In each energy interval, the middle energy are set as the incident energies, and the other secondary energy points are defined based on the method described above. And then calculate the values of scattering probabilities at the secondary energy points. Interpolate the values of scattering probabilities at the same secondary energy points using the special projection interpolation scheme (Muir and Boicourt, 2016). The special projection interpolation scheme is introduced briefly as follows. For a given incident energy E and secondary energy E', the scattering probability $P(E\rightarrow E^{'})$ is represented as

$$P(E\rightarrow E^{'}) = P\left(E_1\rightarrow E_1^{'}\right) + \left(E^{'} - E_1^{'}\right)\cdot\frac{P\left(E_2\rightarrow E_2^{'}\right) - P\left(E_1\rightarrow E_1^{'}\right)}{E_2^{'} - E_1^{'}}, \tag{17}$$

with

$$E - E^{'} = E_1 - E_1^{'} = E_2 - E_2^{'}. \tag{18}$$

where E_1 is the incident energy lower than E; E_2 is the incident energy higher than E; The secondary energies $E_1^{'}$ and $E_2^{'}$ are calculated using Eq. (18). For each energy interval, E_1 equals to the energy of its lower boundary and E_2 equals to the energy of its upper boundary.

3) If the relative error of interpolated probabilities exceeds the given tolerance, the middle incident energy of this energy interval will subdivide this energy interval into two energy intervals. Then, Step 2 is repeated.
4) If the relative error of interpolated probabilities is under the given tolerance for this energy interval which is not generated in Step 1, the lower boundary of this energy interval will be stacked into the final incident energy grid of the $S(\alpha, \beta, T)$ table. Then, skip to the next energy interval and Step 2 is repeated until all the energy intervals are exhausted.
5) If the relative error of interpolated probabilities is under the given tolerance for this energy intervals which is generated in Step 1, the upper boundary of this energy interval will be extended to the next energy point which is the upper boundary of the next energy interval. Then, Step 2 is repeated. The motivation for this operation is to remove the redundant incident energy points from the initial energy grids to reduce the data size of the $S(\alpha, \beta, T)$ table.

After the final incident energy grid of the $S(\alpha, \beta, T)$ table is generated, the scattering kernels of different Legendre orders for each incident energy are evaluated using a semi-analytical integration method (Xu et al., 2019).

2.5. Calculation method of the equally probable cosines

In this section, the calculation method of the equally probable cosines is demonstrated. First of all, the conventional method of calculating equally probable cosines is described in order to explain the proposed method clearly.

The double differential cross section can be expanded using the Legendre polynomials. It is given as

$$\sigma(E\rightarrow E^{'},\mu) = \sum_{n=0}^{\infty}\frac{2n+1}{2}\sigma_n(E\rightarrow E^{'})P_n(\mu), \tag{19}$$

where $\sigma(E\rightarrow E^{'},\mu)$ is the double differential cross section; $\sigma_n(E\rightarrow E^{'})$ is the scattering kernels of nth Legendre order; $P_n(\mu)$ is the Legendre polynomial. Since Eq. (19) is represented as the form of polynomial expansion, $\sigma_n(E\rightarrow E^{'})$ can also be called differential moment. For the convenience of description, the "scattering kernel" is described as "differential moment" in this section.

According to the orthogonality of Legendre polynomials, the differential moments of nth Legendre order are represented as

$$\sigma_n(E\rightarrow E^{'}) = \int_{-1}^{1}\sigma(E\rightarrow E^{'},\mu)P_n(\mu)d\mu. \tag{20}$$

In the conventional method of calculating equally probable cosines, the order of Legendre polynomials represented by n in Eq. (20) is set to 1. Meanwhile, the integral of Eq. (20) is divided by N equally probable parts. Thus, Eq. (20) is rewritten as

$$\sigma_1(E\rightarrow E^{'}) = \sum_{i=1}^{N}\int_{\Delta\mu_i}\sigma(E\rightarrow E^{'},\mu)\mu d\mu, \tag{21}$$

with

$$\int_{\Delta\mu_i}\sigma(E\rightarrow E^{'},\mu)d\mu = \frac{1}{N}\int_{-1}^{1}\sigma(E\rightarrow E^{'},\mu)d\mu = \frac{1}{N}\sigma_0(E\rightarrow E^{'}), \tag{22}$$

where $\Delta\mu_i$ is the ith interval of μ. By using the mean value theorem for integrals, Eq. (21) is rewritten as

$$\begin{aligned}\sigma_1(E\rightarrow E^{'}) &= \sum\nolimits_{i=1}^{N}\int_{\Delta\mu_i}\sigma(E\rightarrow E^{'},\mu)\mu d\mu,\\ &= \sum\nolimits_{i=1}^{N}\overline{\mu}_i\int_{\Delta\mu_i}\sigma(E\rightarrow E^{'},\mu)d\mu = \frac{\sigma_0(E\rightarrow E^{'})}{N}\sum\nolimits_{i=1}^{N}\overline{\mu}_i\end{aligned} \tag{23}$$

where $\overline{\mu}_i$ is the ith equally probable cosine. Therefore, the equally probable cosines are calculated by

$$\overline{\mu}_i = \frac{\int_{\Delta\mu_i}\sigma(E\rightarrow E^{'},\mu)\mu d\mu}{\int_{\Delta\mu_i}\sigma(E\rightarrow E^{'},\mu)d\mu} = N\frac{\int_{\Delta\mu_i}\sigma(E\rightarrow E^{'},\mu)\mu d\mu}{\sigma_0(E\rightarrow E^{'})}. \tag{24}$$

From the above equations, it can be observed that the double differential cross sections $\sigma(E\rightarrow E^{'},\mu)$ are always desired in the conventional calculation method.

In the present work, the calculation of the double differential cross sections is avoided. A calculation method is proposed to calculate the equally probable cosines by utilizing the differential moments. According to the mean value theorem for integrals, Eq. (20) can be represented as

$$\sigma_n(E\rightarrow E^{'}) = \sum_{i}^{N}P_n(\overline{\mu}_i)\int_{\Delta\mu_i}\sigma(E\rightarrow E^{'},\mu)d\mu = \frac{\sigma_0(E\rightarrow E^{'})}{N}\sum_{i=1}^{N}P_n(\overline{\mu}_i), \tag{25}$$

where $\overline{\mu}_i$ is the unknown quantities. There are N unknown quantities $\overline{\mu}_i$ which can be solved by N equations. For different Legendre order n, Eq. (25) can be rewritten with different form. Thus, these N equations for solving $\overline{\mu}_i$ are obtained by rewritten Eq. (25) from 1st order to N^{th} order.

For the case that N equals to 0, the number of equally probable cosines is given arbitrarily to represent the isotropy of scattering angle. It is unnecessary to establish the set of equations and the equally probable cosines are obtained directly.

For the case that N equals to 1, the number of equally probable cosines is 1. The set of equations is given by

$$\sigma_0(E\rightarrow E^{'})\cdot\overline{\mu}_1 = \sigma_1(E\rightarrow E^{'}). \tag{26}$$

For the case that N equals to 2, the number of equally probable cosines is 2. The set of equations is given by

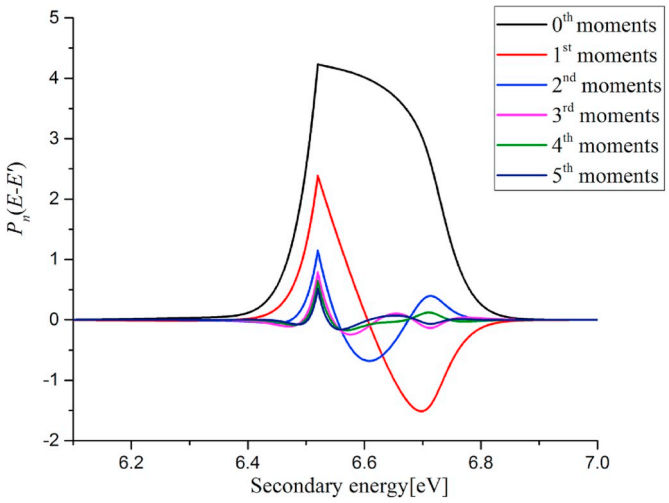

Fig. 7. The differential moments of the first six Legendre order of ^{238}U for the incident energy of 6.52 eV at 1000 K.

$$\begin{cases} \sigma_0(E\to E^{'})\cdot\frac{1}{2}(\overline{\mu}_1+\overline{\mu}_2)=\sigma_1(E\to E^{'}) \\ \sigma_0(E\to E^{'})\cdot\frac{1}{2}\left(\frac{1}{2}\left(3\overline{\mu}_1{}^2-1\right)+\frac{1}{2}\left(3\overline{\mu}_2{}^2-1\right)\right)=\sigma_2(E\to E^{'}) \end{cases}, \tag{27}$$

where the constraint is

$$-1<\overline{\mu}_1<\overline{\mu}_2<1. \tag{28}$$

For the case that N equals to 3, the number of equally probable cosines is 3. The set of equations is given by

$$\begin{cases} \sigma_0(E\to E^{'})\cdot\frac{1}{3}(\overline{\mu}_1+\overline{\mu}_2+\overline{\mu}_3)=\sigma_1(E\to E^{'}) \\ \sigma_0(E\to E^{'})\cdot\frac{1}{3}\left(\frac{1}{2}\left(3\overline{\mu}_1{}^2-1\right)+\frac{1}{2}\left(3\overline{\mu}_2{}^2-1\right)++\frac{1}{2}\left(3\overline{\mu}_3{}^2-1\right)\right)=\sigma_2(E\to E^{'}) \\ \sigma_0(E\to E^{'})\cdot\frac{1}{3}\left(\frac{1}{2}\left(5\overline{\mu}_1{}^3-3\overline{\mu}_1\right)+\frac{1}{2}\left(5\overline{\mu}_2{}^3-3\overline{\mu}_2\right)++\frac{1}{2}\left(5\overline{\mu}_3{}^3-3\overline{\mu}_3\right)\right)=\sigma_3(E\to E^{'}) \end{cases}, \tag{29}$$

where the constraint is

$$-1<\overline{\mu}_1<\overline{\mu}_2<\overline{\mu}_3<1. \tag{30}$$

For the case of larger n, the set of nonlinear equations is established by using Legendre polynomials to rewrite Eq. (25) from 1st to N^{th} Legendre order in turn. From Eq. (26) and Eq. (29), it can be seen that the complexity of the set of nonlinear equations increases as n increases. The first two order of equation sets can be solved by the undetermined coefficient method, and the high order of equation sets can be solved by a numerical method such as Newton's method.

Fig. 7 gives the differential moments of the first six Legendre order of ^{238}U for the incident energy of 6.52 eV at 1000 K. It can be seen that the absolute values of scattering probabilities from 3rd to higher Legendre order are much smaller in comparison to those of 0th Legendre moment, which implies that the angular anisotropy of scattered neutrons affected by RESK is not very strong. As a result, the maximum Legendre order is truncated to the 2nd order in this study. By solving the quadratic equation derived from Eq. (27), the final equally probable cosines are obtained.

After the nuclear data processing, the data of $S(\alpha, \beta, T)$ table is output into derived files which are the "point-ENDF" (PENDF) files. The PENDF files can be read by the nuclear data processing codes for generating the ACE-format libraries.

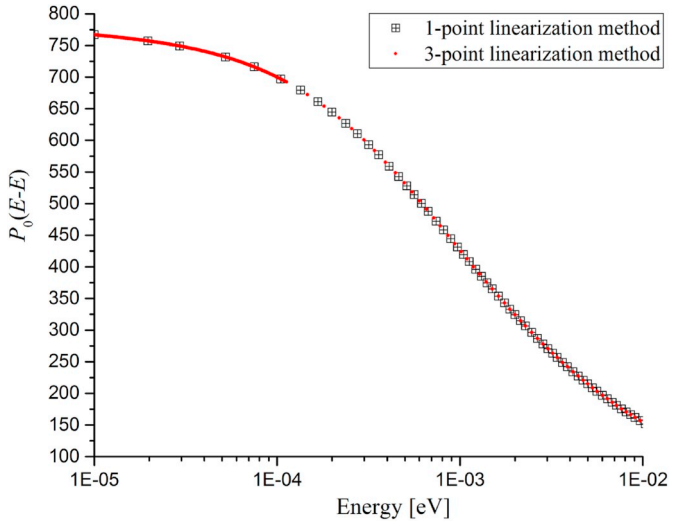

Fig. 8. The self-scattering probabilities of 0th Legendre order of ^{238}U at 900 K for the incident energy from 1E-5 eV to 1E-2 eV.

3. Numerical results

3.1. Performance of the multi-point linearization method

In this work, 3 secondary points in all are defined in the multi-point linearization method, which can be called 3-point linearization method. Using the 3-point linearization method, the incident energy grid of the $S(\alpha, \beta, T)$ table for ^{238}U at 900 K has 1333 points from 1E-5 eV–100 eV, while there are 817 energy points are generated, when the previous linearization method is used. It should be noted that the previous linearization method is equivalent to the 1-point linearization method. Fig. 8 and Fig. 9 show the self-scattering probabilities of 0th Legendre order of ^{238}U at 900 K for the incident energy from 1E-5 eV to 1E-2 eV, and from 3 eV to 8 eV, respectively. And the incident energy points corresponding to the self-scattering probabilities construct the incident energy grid of the $S(\alpha, \beta, T)$ table.

It can be seen that when the 3-point linearization method is applied, the incident energy grid is refined within the thermal energy range and the incident energy gird within the epi-thermal energy range keep unchanged.

Meanwhile, the number incident energy points for different number of secondary points are listed in Table 1. It can be noticed that the number of incident energy points increases when more secondary points are set. Consequently, the processing time will increase. The ratio of the processing time between 1-point and 3-point linearization method is basically equal to that of the number of incident energy points between the two methods.

The scattering kernels for the incident energy of 2E-5 eV and 4E-5 eV gotten by the multi-point linearization method are respectively shown in

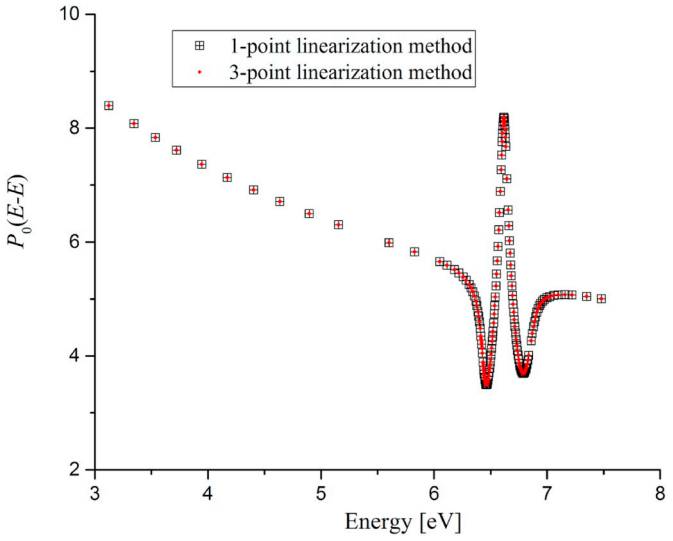

Fig. 9. The self-scattering probabilities of 0th Legendre order of ^{238}U at 900 K for the incident energy from 3 eV to 8 eV.

Table 1
The number incident energy points for different number of secondary points.

Number of secondary points in multi-point linearization method	Number of incident energy points
1-point linearization method	871
3-point linearization method	1333

Fig. 10 and Fig. 11. The interpolated value is obtained using the interpolation table of scattering kernel based on the 3-point linearization method. As shown in Figs. 10 and 11, the absolute value of maximum relative error of interpolation for the scattering kernel for the incident energy of 2E-5 eV is 0.04%. The absolute maximum relative error of interpolation for the scattering kernel for the incident energy of 4E-5 eV is 0.21%. The proposed method can guarantee the interpolation precision, and improve the robustness.

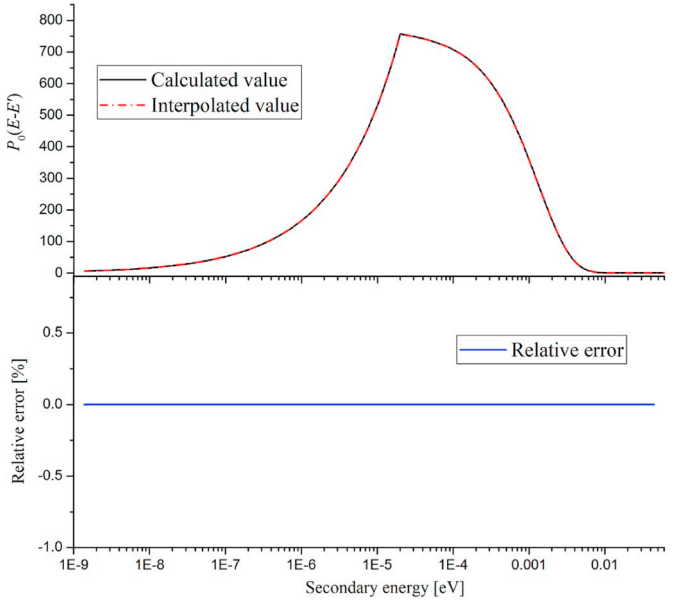

Fig. 10. The comparison of the scattering kernel of ^{238}U for the incident energy of 2E-5 eV.

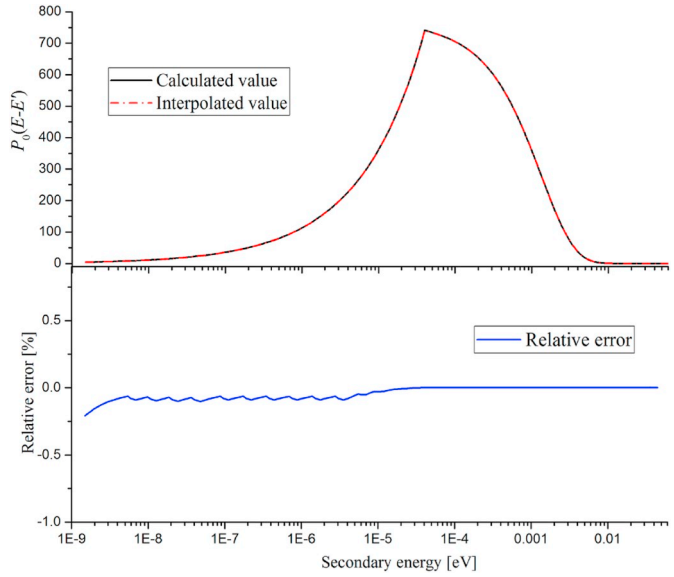

Fig. 11. The comparison of the scattering kernel of ^{238}U for the incident energy of 4E-5 eV.

3.2. Verification of the up-scattering probabilities

The up-scattering probabilities at different incident energies for ^{238}U, ^{235}U and ^{238}Pu are also compared. The reference solution is given by the paper(Ghrayeb et al., 2014). Table 2, Table 3 and Table 4 give the comparison of the up-scattering probabilities for ^{238}U, ^{235}U and ^{238}Pu,

Table 2
Up-scattering probabilities of^{238}U.

Incident energy(eV)	Temperature/K	Up-scattering probability-Ref./%	Up-scattering probability/%	Relative Diff/%
6.52	300	62.17	62.28	0.18
	600	82.84	82.83	−0.01
	1000	84.45	84.32	−0.15
7.2	300	16.58	16.50	−0.48
	600	23.59	23.50	−0.38
	1000	28.20	28.12	−0.28

Table 3
Up-scattering probabilities of^{235}U.

Incident energy(eV)	Temperature/K	Up-scattering probability-Ref./%	Up-scattering probability/%	Relative Diff/%
6.0	300	18.71	18.62	−0.48
	600	25.93	25.85	−0.31
	1000	30.66	30.59	−0.23
6.8	300	17.32	17.23	−0.52
	600	24.55	24.47	−0.33
	1000	29.33	29.27	−0.20

Table 4
Up-scattering probabilities of^{238}Pu.

Incident energy(eV)	Temperature/K	Up-scattering probability-Ref./%	Up-scattering probability/%	Relative Diff/%
18.45	300	20.52	20.21	−1.51
	600	29.20	28.82	−1.30
	1000	34.57	34.17	−1.16
19.4	300	7.66	7.61	−0.65
	600	13.48	13.40	−0.59
	1000	18.54	18.45	−0.49

Table 5
Eigenvalues based on different Legendre orders

UO_2 (wt. %)	0^{th} order	0^{th}-1st orders	0^{th}-2nd orders
0.71	0.66540 (0.00005)	0.66551 (0.00005)	0.66550 (0.00005)
1.60	0.96043 (0.00007)	0.96055 (0.00006)	0.96059 (0.00007)
2.40	1.09881 (0.00007)	1.09896 (0.00007)	1.09892 (0.00007)
3.10	1.17647 (0.00008)	1.17660 (0.00008)	1.17668 (0.00008)
3.90	1.23928 (0.00007)	1.23940 (0.00007)	1.23946 (0.00007)
4.50	1.27480 (0.00007)	1.27487 (0.00007)	1.27481 (0.00007)
5.00	1.29901 (0.00008)	1.29910 (0.00008)	1.29910 (0.00008)

Table 6
Comparision of eigenvalues for the Mosteller UOX fuel benchmark at 600 K.

UO_2 (wt. %)	Method-1	Method-2	Method-3	Diff.-1/ pcm	Diff.-2/ pcm
0.71	0.66606 (0.00005)	0.66546 (0.00005)	0.66550 (0.00005)	4	−56
1.60	0.96128 (0.00007)	0.96059 (0.00006)	0.96059 (0.00007)	0	−69
2.40	1.09954 (0.00007)	1.09862 (0.00007)	1.09892 (0.00007)	30	−62
3.10	1.17760 (0.00008)	1.17680 (0.00008)	1.17668 (0.00008)	−12	−92
3.90	1.24030 (0.00007)	1.23947 (0.00007)	1.23946 (0.00007)	−1	−84
4.50	1.27570 (0.00007)	1.27483 (0.00007)	1.27481 (0.00007)	−2	−89
5.00	1.30012 (0.00008)	1.29927 (0.00008)<	1.29910 (0.00008)	−17	−102

respectively. It can be concluded that the up-scattering probabilities agree well with the reference.

3.3. Analysis for the impact on the eigenvalues caused by the higher order moments

According to Fig. 7, the absolute values of the higher order moments cannot be ignored. It means that the angular anisotropy of scattered neutron at some incident energies are considerable. Therefore, the impact on the eigenvalues caused by the higher order moments should be analyzed.

Three sets of ACE libraries are generated, where the $S(\alpha, \beta, T)$ tables are processed based on the moment of the first (0^{th}) order, the first two (0^{th}-1st) and the first three (0^{th}-2nd) orders, respectively. The UOX fuel problems at 600 K in Mosteller benchmarks are used for the analysis (Mosteller, 2006). The results are given in Table 5. It can be seen that the eigenvalues based on the moments of the first two (0^{th}-1st) and three (0^{th}-2nd) orders are almost same, which means the convergence is reached. The eigenvalue of all problems based on the moments of the first order are smaller than the converged values about 10 pcm, which means that 0^{th} order is not high enough to let the eigenvalues converge. Thus, the moments of first three (0^{th}-2nd) orders are sufficient to generate the $S(\alpha, \beta, T)$ tables and ACE libraries.

3.4. Verification of the S(α, β, T) tables

The proposed processing method of generating $S(\alpha, \beta, T)$ tables considering the resonance scattering is tested in this subsection. The methods described in Section 2 have been implemented into the nuclear data processing code NECP-Atlas (Zu et al., 2019). And the $S(\alpha, \beta, T)$

Table 7
Comparision of eigenvalues for the Mosteller UOX fuel benchmark at 900 K.

UO_2 (wt. %)	Method-1	Method-2	Method-3	Diff.-1/ pcm	Diff.-2/ pcm
0.71	0.66050 (0.00005)	0.65956 (0.00005)	0.65939 (0.00005)	−17	−111
1.60	0.95352 (0.00007)	0.95194 (0.00007)	0.95199 (0.00007)	5	−153
2.40	1.09077 (0.00008)	1.08889 (0.00008)	1.08902 (0.00008)	13	−175
3.10	1.16828 (0.00008)	1.16637 (0.00007)	1.16645 (0.00008)	8	−183
3.90	1.23044 (0.00008)	1.22867 (0.00008)	1.22856 (0.00008)	−11	−188
4.50	1.26583 (0.00007)	1.26381 (0.00007)	1.26384 (0.00007)	3	−199
5.00	1.28996 (0.00008)	1.28799 (0.00008)	1.28799 (0.00008)	0	−197

Table 8
Comparision of eigenvalues for the Mosteller Reactor-Recycle MOX fuel benchmark at 600 K.

PuO_2 (wt. %)	Method-1	Method-2	Method-3	Diff.-1/ pcm	Diff.-2/ pcm
1.00	0.94724 (0.00007)	0.94629 (0.00007)	0.94629 (0.00007)	−5	−100
2.00	1.02350 (0.00008)	1.02220 (0.00008)	1.02220 (0.00008)	9	−121
4.00	1.07867 (0.00007)	1.07735 (0.00007)	1.07735 (0.00007)	10	−122
6.00	1.10715 (0.00007)	1.10608 (0.00008)	1.10608 (0.00008)	8	−99
8.00	1.13048 (0.00007)	1.12938 (0.00007)	1.12938 (0.00007)	−13	−123

Table 9
Comparision of eigenvalues for the Mosteller Reactor-Recycle MOX fuel benchmark at 900 K.

PuO_2 (wt. %)	Method-1	Method-2	Method-3	Diff.-1/ pcm	Diff.-2/ pcm
1.00	0.93725 (0.00007)	0.93536 (0.00007)	0.93551 (0.00007)	15	−174
2.00	1.01249 (0.00008)	1.01032 (0.00008)	1.01043 (0.00008)	11	−206
4.00	1.06722 (0.00007)	1.06510 (0.00007)	1.06492 (0.00007)	−18	−230
6.00	1.09543 (0.00008)	1.09379 (0.00008)	1.09362 (0.00008)	−17	−181
8.00	1.11890 (0.00007)	1.11685 (0.00007)	1.11682 (0.00007)	−3	−208

Table 10
Comparision of eigenvalues for the Mosteller Weapon-Grade MOX fuel benchmark at 600 K.

PuO_2 (wt. %)	Method-1	Method-2	Method-3	Diff.-1/ pcm	Diff.-2/ pcm
1.00	1.09169 (0.00007)	1.09092 (0.00007)	1.09106 (0.00007)	14	−63
2.00	1.18239 (0.00007)	1.18129 (0.00007)	1.18136 (0.00007)	7	−103
4.00	1.25115 (0.00006)	1.25001 (0.00007)	1.24989 (0.00007)	−12	−126
6.00	1.28770 (0.00007)	1.28673 (0.00007)	1.2867 (0.00007)	−1	−98

Table 11
Comparision of eigenvalues for the Mosteller Weapon-Grade MOX fuel benchmark at 900 K.

PuO_2 (wt. %)	Method-1	Method-2	Method-3	Diff.-1/ pcm	Diff.-2/ pcm
1.00	1.08239 (0.00007)	1.08042 (0.00007)	1.08053 (0.00007)	11	−186
2.00	1.17143 (0.00007)	1.16905 (0.00007)	1.16928 (0.00006)	23	−215
4.00	1.23895 (0.00007)	1.23674 (0.00007)	1.23689 (0.00007)	15	−206
6.00	1.27542 (0.00006)	1.27325 (0.00007)	1.27333 (0.00007)	8	−209

Table 12
Comparision of eigenvalues for the BEAVRS benchmark.

Type of assembly	Method-1	Method-2	Method-3	Diff.-1/ pcm	Diff.-2/ pcm
Fuel assembly	1.17363 (0.00004)	1.17180 (0.00004)	1.17179 (0.00004)	−1	−183
Rod-cluster-control assembly	0.83398 (0.00004)	0.83274 (0.00004)	0.83261 (0.00004)	−13	−137

Table 13
Information of the ICSBEP benchmark.

ICSBEP label	Short name	Identification
PU-SOL-THERM-001	PST001	Pu-Solution-Thermal (Light water-moderated)
HEU-SOL-THERM-001	HST001	High enriched U-Solution-Thermal (Light water-moderated)
IEU-SOL-THERM-004	IST004	Intermediate enriched U-Solution-Thermal (Light water, BeO-moderated)
MIX-COMP-THERM-013	MCT013	Mixed U, Pu-Compound-Thermal (polyethylene-moderated)
MIX-SOL-THERM-003	MST003	Mixed U, Pu-Solution-Thermal (Light water, polyethylene-moderated)

tables considering the RESK used in the neutronics calculations is generated by NECP-Atlas based on ENDF/B-VII.1.

The Monte Carlo code OpenMC (Romano et al., 2015), which can treat the RESK through the DBRC approach, is used as the reference to calculate some benchmarks. In order to verify the proposed processing method of generating $S(\alpha, \beta, T)$ tables and show the effect on eigenvalues caused by RESK, three different kinds of calculations are performed. The first is not using any $S(\alpha, \beta, T)$ table for all heavy nuclides (denoted as Method-1); the second is applying the DBRC approach to all heavy nuclides (denoted as Method-2); the last is using the $S(\alpha, \beta, T)$ tables generated by NECP-Atlas for all heavy nuclides (denoted as Method-3).

Two kinds of comparison are performed. One is comparing the difference of eigenvalues between Method-3 and Method-2, which is to verify the precision of the proposed method (denoted as Diff.-1); the other is comparing the difference between Method-3 and Method-1, which is to show the effect on eigenvalues caused by RESK (denoted as Diff.-2).

3.4.1. Mosteller pin-cell benchmark

The Mosteller benchmarks are calculated, including UOX fuel, Reactor-Recycle MOX fuel and Weapon-Grade MOX fuel problems (Mosteller, 2006). Two cases of fuel temperature are analyzed, i.e. 600 K and 900 K. The results of the eigenvalues for different cases are summarized in Tables 6-11. In the tables, From Diff.-1, it is proved that the proposed processing method of generating $S(\alpha, \beta, T)$ can get comparable results with DBRC approach. From Diff.-2, it can be seen that the

Table 14
Comparision of eigenvalues for the ICSBEP benchmark.

Short name	Method-1	Method-2	Method-3	Diff.-1/pcm	Diff.-2/pcm
PST001001	1.00842 (0.00004)	1.00836 (0.00004)	1.00838 (0.00004)	2	−4
PST001002	1.00990 (0.00004)	1.00983 (0.00004)	1.00983 (0.00004)	0	−7
PST001003	1.01275 (0.00003)	1.01261 (0.00003)	1.01265 (0.00004)	4	−10
PST001004	1.00787 (0.00004)	1.00763 (0.00004)	1.00767 (0.00004)	4	−20
PST001005	1.01138 (0.00004)	1.01112 (0.00004)	1.01115 (0.00004)	3	−23
PST001006	1.01528 (0.00004)	1.01493 (0.00004)	1.01491 (0.00004)	−2	−37
HST001001	0.96118 (0.00004)	0.96120 (0.00004)	0.96114 (0.00004)	−6	−4
HST001002	0.96997 (0.00004)	0.96999 (0.00004)	0.96990 (0.00004)	−9	−7
HST001003	0.99174 (0.00004)	0.99176 (0.00004)	0.99177 (0.00004)	1	3
HST001004	1.00530 (0.00004)	1.00528 (0.00004)	1.00530 (0.00004)	2	0
HST001005	0.96571 (0.00004)	0.96570 (0.00004)	0.96569 (0.00004)	−1	−2
IST004001	0.93459 (0.00004)	0.93421 (0.00005)	0.93422 (0.00004)	1	−37
MCT013001	1.00478 (0.00004)	1.00356 (0.00004)	1.00362 (0.00004)	6	−116
MCT013002	1.00576 (0.00004)	1.00444 (0.00004)	1.00451 (0.00004)	7	−125
MCT013003	1.00574 (0.00004)	1.00454 (0.00004)	1.00454 (0.00004)	0	−120
MCT013004	1.00593 (0.00004)	1.00464 (0.00004)	1.00471 (0.00004)	7	−122
MCT013005	1.00589 (0.00004)	1.00464 (0.00004)	1.00461 (0.00004)	−3	−128
MCT013006	1.00434 (0.00004)	1.00309 (0.00004)	1.00295 (0.00004)	−14	−139
MCT013007	1.00393 (0.00004)	1.00262 (0.00004)	1.00270 (0.00004)	8	−123
MCT013008	1.00326 (0.00004)	1.00192 (0.00004)	1.00193 (0.00004)	1	−133
MCT013009	1.00168 (0.00003)	1.00032 (0.00004)	1.00035 (0.00003)	3	−133
MCT013010	1.00239 (0.00004)	1.00101 (0.00004)	1.00107 (0.00004)	6	−132
MCT013011	0.96366 (0.00004)	0.96250 (0.00004)	0.96251 (0.00004)	1	−115
MCT013012	1.00035 (0.00004)	0.99906 (0.00004)	0.99902 (0.00004)	−4	−133
MCT013013	1.00254 (0.00004)	1.00131 (0.00004)	1.00130 (0.00004)	1	−124
MCT013014	1.00054 (0.00004)	0.99924 (0.00004)	0.99929 (0.00004)	−4	−125
MCT013015	0.99977 (0.00004)	0.99852 (0.00004)	0.99847 (0.00004)	−1	−130
MST003001	1.00516 (0.00004)	1.00449 (0.00004)	1.00460 (0.00004)	11	−56
MST003002	0.99649 (0.00004)	0.99598 (0.00004)	0.99597 (0.00004)	−1	−52
MST003003	0.99285 (0.00004)	0.99227 (0.00003)	0.99232 (0.00004)	5	−53
MST003004	0.98586 (0.00004)	0.98525 (0.00004)	0.98526 (0.00004)	1	−60
MST003005	1.01538 (0.00004)	1.01524 (0.00004)	1.0152 0(0.00004)	−4	−18
MST003006	1.01486 (0.00004)	1.01464 (0.00004)	1.01465 (0.00004)	1	−21
MST003007	1.00809 (0.00004)	1.0079 6(0.00005)	1.00796 (0.00004)	0	−13
MST003008	1.04477 (0.00004)	1.0447 4(0.00004)	1.04472 (0.00004)	−2	−5
MST003009	1.03754 (0.00004)	1.03755 (0.00004)	1.03752 (0.00004)	−3	−2
MST003010	1.04218 (0.00004)	1.04217 (0.00004)	1.04213 (0.00004)	−4	−5

eigenvalues decrease to different degrees depending on the fuel types and temperature, due to RESK.

3.4.2. Assembly problems in BEAVRS benchmark

Two assembly problems in BEAVRS benchmark (Horelik and Herman, 2012) are calculated including a UO_2 fuel assembly with 3.1% enrichment and a borosilicate-glass rod-cluster-control assembly with the all-control-rod-in condition. The results of the eigenvalues at 900 K are represented in Table 12. It is observed that the eigenvalues based on the $S(\alpha, \beta, T)$ tables and those based on the DBRC approach agree well with each other, and the eigenvalues decrease greatly for the two types of assembly.

3.4.3. ICSBEP benchmark

To verify the applicability of the $S(\alpha, \beta, T)$ tables for the applications other than the conventional pressurized water reactor problems, 37 thermal-spectrum benchmarks in ICSBEP benchmark (OECD-NEA, 2006) are analyzed. The information of the benchmarks is listed in Table 13. To make the effect of RESK on eigenvalues more obvious, the temperatures of the materials including heavy nuclides in the benchmarks are set to be 900 K artificially with the geometries and the types of materials unchanged. The calculation results are listed in Table 14. From Diff.-1, the $S(\alpha, \beta, T)$ tables has good agreement with DBRC approach. From Diff.-2, it can be found that the eigenvalues decrease in varying degrees for different benchmarks.

4. Conclusion

A new processing method for generating $S(\alpha, \beta, T)$ tables is proposed, which can exactly account for RESK. In this method, a multi-point linearization method is developed to improve the precision of the values of scattering probabilities at different secondary energies obtained by interpolation. The equally probable cosines are evaluated by solving the sets of nonlinear equations which are established by the differential moments and Legendre polynomials. The $S(\alpha, \beta, T)$ tables generated by the above methods are supplied to the Monte Carlo code OpenMC, to analyze the Mosteller pin-cell benchmark, assembly problems in BEAVRS benchmark and ICSBEP benchmarks. The numerical results shows that the proposed $S(\alpha, \beta, T)$ tables can provide comparable results with the Doppler broadening rejection correction approach. The proposed methods can produce the accurate $S(\alpha, \beta, T)$ tables in ACE format for the Monte Carlo codes to accurately threat RESK without modifying the source code of the used Monte Carlo codes.

Acknowledgement

This work was supported by The National Natural Science Foundation of China (No. 11605128, 11735011).

Appendix A. Supplementary data

Supplementary data to this article can be found online at https://doi.org/10.1016/j.pnucene.2020.103262.

References

Becker, B., 2010. On the Influence of the Resonance Scattering Treatment in Monte Carlo Codes on High Temperature Reactor Characteristics. Ph.D. thesis, University of Stuttgart, Germany.
Becker, B., Dagan, R., Lohnert, G., 2009. Proof and implementation of the stochastic formula for ideal gas, energy dependent scattering kernel. Ann. Nucl. Energy 36, 470–474.
Dagan, R., 2005. On the use of S(α,β) tables for nuclides with well pronounced resonances. Ann. Nucl. Energy 32, 367–377.
Dagan, R., et al., 2011. Modelling a resonance dependent angular distribution via DBRC in Monte Carlo Codes. J. Kor. Phys. Soc. 59 (2), 983–986.
Ghrayeb, S.Z., et al., 2014. Multi-group formulation of the temperature-dependent resonance scattering model and its impact on reactor core parameters. Ann. Nucl. Energy 63, 751–762.
He, Q., et al., 2016. Neutron up-scattering effect in refined energy group structure. In: Proceedings of the 2016 24th International Conference on Nuclear Engineering ICONE24, Charlotte. North Carolina, USA, JUNE 26-30, 2016.
Horelik, N., Herman, B., 2012. Benchmark for Evaluation and Validation of Reactor Simulations. MIT Computational Reactor Physics Group.
Lee, D., Smith, K., Rhodes, J., 2008. The impact of ^{238}U resonance elastic scattering approximations on thermal reactor Doppler reactivity. In: International Conference on Reactor Physics, Nuclear Power: A Sustainable Resource. Interlaken, Switzerland. September 14–19, 2008.
Mori, T., Nagaya, Y., 2009. Comparison of resonance elastic scattering models newly implemented in MVP continuous-energy Monte Carlo code. J. Nucl. Sci. Technol. 46 (8), 793–798.
Mosteller, R.D., 2006. Computational benchmark for the Doppler reactivity defect, Tech. Rep. LA-UR-06-2968. Los Alamos Natl. Lab. 1–20.
Muir, W.D., Boicourt, R.M., et al., 2016. 2016. The NJOY Nuclear Data Processing System, Version 2016. LA-UR- 17-20093. Los Alamos National Laboratory, Los Alamos, USA.
Oecd-Nea, 2006. International Handbook of Evaluated Criticality Safety Benchmark Experiments. OECD-NEA, UK.
Ouisloumen, M., Ougouag, A.M., Ghrayeb, S.Z., 2015. Anisotropic elastic resonance scattering model for the neutron transport equation. Nucl. Sci. Eng. 179, 59–84.
Ouisloumen, M., Sanchez, R., 1991. A model for neutron scattering off heavy isotopes that accounts for thermal agitation effects. Nucl. Sci. Eng. 107, 189–200.
Romano, P.K., et al., 2015. OpenMC: a state-of-the-art Monte Carlo code for research and development. Ann. Nucl. Energy 82, 90–97.
Rothenstein, W., 2004. Proof of the formula for the ideal gas scattering kernel for nuclides with strongly energy dependent scattering cross sections. Ann. Nucl. Energy 31, 9–23.
Walsh, J.A., et al., 2014. Accelerated sampling of the free gas resonance elastic scattering kernel. Ann. Nucl. Energy 69, 116–124.
Xu, J., et al., 2019. Development and verification of resonance elastic scattering kernel processing module in nuclear data processing code NECP-Atlas. Prog. Nucl. Energy 110, 301–310.
Zoia, A., Brun, E., Jouanne, C., Malvagi, F., 2013. Doppler broadening of neutron elastic scattering kernel in TRIPOLI-4. Ann. Nucl. Energy 54, 218–226.
Zu, T., et al., 2019. 2019. NECP-Atlas: a new nuclear data processing code. Ann. Nucl. Energy 123, 153–161.